Well-balanced schemes for the Euler equations with gravitation

R. Käppeli [*], S. Mishra

Seminar for Applied Mathematics (SAM), Department of Mathematics, ETH Zürich, CH-8092 Zürich, Switzerland

A R T I C L E   I N F O

A B S T R A C T

Well-balanced high-order finite volume schemes are designed to approximate the Euler equations with gravitation. The schemes preserve discrete equilibria, corresponding to a large class of physically stable hydrostatic steady states. Based on a novel local hydrostatic reconstruction, the derived schemes are well-balanced for any consistent numerical flux for the Euler equations. The form of the hydrostatic reconstruction is both very simple and computationally efficient as it requires no analytical or numerical integration. Moreover, as required by many interesting astrophysical scenarios, the schemes are applicable beyond the ideal gas law. Both first- and second-order accurate versions of the schemes and their extension to multi-dimensional equilibria are presented. Several numerical experiments demonstrating the superior performance of the well-balanced schemes, as compared to standard finite volume schemes, are also presented.

1. Introduction

1.1. Systems of balance laws

Many interesting physical phenomena are modeled by the Euler equations with gravitational source terms. Examples include the study of atmospheric phenomena that are essential in numerical weather prediction and in climate modeling as well as in a wide variety of contexts in astrophysics such as modeling solar climate or simulating supernova explosions. The Euler equations with gravitational source terms express the conservation of mass, momentum and energy and are given by,

$$\frac{\partial \rho}{\partial t} + \nabla \cdot (\rho \boldsymbol{v}) = 0, \tag{1.1}$$

$$\frac{\partial \rho \boldsymbol{v}}{\partial t} + \nabla \cdot (\boldsymbol{v} \rho \boldsymbol{v}) + \nabla p = -\rho \nabla \phi, \tag{1.2}$$

$$\frac{\partial E}{\partial t} + \nabla \cdot \left[(E + p) \boldsymbol{v} \right] = -\rho \boldsymbol{v} \cdot \nabla \phi. \tag{1.3}$$

Here, ρ is the mass density, $\boldsymbol{v}$ the velocity and

$$E = \rho e + \frac{\rho}{2} v^2,$$

the total energy being the sum of internal and kinetic energy. The pressure p is related to the density and specific internal energy through an equation of state $p = p(\rho, e)$.

---

* Corresponding author.
  E-mail address: roger.kaeppeli@sam.math.ethz.ch (R. Käppeli).

The right hand side of the momentum and energy conservation equations models the effect of gravitational forces onto the conserved variables in terms of the gravitational potential ϕ. This potential can be a given function such as the linear gravitational potential, $\phi(x, y, z) = gz$ (with z being the vertical spatial coordinate) that arises in atmospheric modeling or it can also be determined by the Poisson equation

$$\nabla^2 \phi = 4\pi G \rho, \tag{1.4}$$

in the case of self-gravity, which is very relevant in an astrophysical context.

The Euler equations with gravitation (1.1)–(1.3) are a prototypical example for a system of balance laws,

$$\mathbf{U}_t + \nabla \cdot \big(\mathbf{F}(\mathbf{U})\big) = \mathbf{S}(\mathbf{U}), \tag{1.5}$$

with $\mathbf{U}, \mathbf{F}$ and $\mathbf{S}$ being the vector of unknowns, the flux and the source, respectively. The special case of $\mathbf{S} \equiv 0$ is termed a conservation law. It is well known [1] that solutions of systems of conservation (balance) laws contain discontinuities in the form of shock waves and contact discontinuities, even when the initial data are smooth. Hence, the solutions of the balance law (1.5) are interpreted in the sense of distributions. Furthermore, these weak solutions may not be unique. Additional admissibility criteria or *entropy conditions* need to be imposed in order to select the physically relevant solution.

Numerical methods for system of conservation (balance) laws are in a mature stage of development. Among the most popular discretization frameworks are the so-called finite volume methods [2], where the cell averages of the unknown are evolved in terms of numerical fluxes. The numerical fluxes are determined by approximate or exact solutions of Riemann problems at each cell interface, in the normal direction. Higher order spatial accuracy is provided by suitable non-oscillatory reconstruction procedures such as TVD, ENO or WENO reconstructions. An alternative for high-order spatial accuracy relies on the Discontinuous Galerkin (DG) finite element method. Higher order time integration is performed by using strong stability preserving (SSP) Runge–Kutta methods. This framework has resulted in efficient resolutions of very complex physical phenomena modeled by system of conservation (balance) laws.

1.2. Role of steady states

An interesting issue that arises when the analysis and numerical approximation of systems of balance laws (1.5) is performed, is the presence of non-trivial steady states. Such steady states (stationary solutions) are defined by the *flux-source balance*:

$$\nabla \cdot \big(\mathbf{F}(\mathbf{U})\big) = \mathbf{S}(\mathbf{U}). \tag{1.6}$$

A particular example is provided by the hydrostatic steady state for the Euler equations with gravitation (1.1)–(1.3). In this stationary solution, the velocity is zero, i.e. $\boldsymbol{v} \equiv 0$ and the pressure exactly balances the gravitational force:

$$\nabla p = -\rho \nabla \phi. \tag{1.7}$$

The above steady state models the so-called *mechanical equilibrium* and is incomplete to some extent as the density and pressure stratifications are not uniquely specified. Another thermodynamic variable is needed (e.g. entropy or temperature) to uniquely determine the equilibrium. However, arbitrary entropy or temperature profiles may not result in physically stable equilibria. For stability, the gradient of the entropy or the temperature profile must fulfill certain criteria (see e.g. [3]). Two important classes of stable hydrostatic equilibria are characterized by constant entropy, i.e. isentropic, and constant temperature, i.e. isothermal, respectively.

As a concrete astrophysically relevant example of a stable stationary state, we assume constant entropy and use the following thermodynamic relation

$$\mathrm{d}h = T\,\mathrm{d}s + \frac{\mathrm{d}p}{\rho}, \tag{1.8}$$

where h is the specific enthalpy

$$h = e + \frac{p}{\rho}, \tag{1.9}$$

T the temperature and s the specific entropy. Then we can write (1.7) for the isentropic case ($\mathrm{d}s = 0$) as

$$\frac{1}{\rho}\nabla p = \nabla h = -\nabla \phi. \tag{1.10}$$

The last equation can then be trivially integrated to obtain,

$$h + \phi = const. \tag{1.11}$$

The importance of steady states such as the above equilibrium lies in the fact that in many situations of interest, the dynamics is realized as a perturbation of the steady states. As examples, consider the simulation of small perturbations on a

gravitationally stratified atmosphere such as those arising in numerical weather prediction [4] and the simulation of waves in stellar atmospheres [5,6].

Another situation where near steady state flows are of great interest occurs in astrophysics, in particular in the simulation of core-collapse supernova explosions, where the nascent neutron star slowly settles to an equilibrium (with a dynamical time scale of few ms) albeit the explosion, taking place in a highly dynamic environment just above the nascent neutron star, does not set in for another few hundreds of ms [7]. Here, the interest is in accurate long (compared to the characteristic dynamic time scale on which the steady state reacts to perturbations) term simulations of near stationary states.

1.3. Well-balanced schemes

The numerical approximation of near steady flows is quite challenging as standard finite volume schemes do not necessarily satisfy a discrete version of the flux-source balance (1.6). Consequently, the resulting steady states are not preserved exactly by the scheme but are approximated with an error that is proportional to the truncation error. So if one is interested in small perturbations of the equilibrium, the numerical resolution has to be increased to the point where the ratio between the magnitude of the truncation errors and the perturbations becomes small enough. In multi-dimensional simulations the needed resolution for standard schemes then becomes prohibitively large.

In order to overcome this challenge, an additional design principle was introduced by Greenberg and Leroux [8], leading to the requirement of a *well-balanced scheme*, i.e. a finite volume scheme that satisfies a discrete version of the flux-source balance (1.6) and can preserve a discrete steady state of interest, up to machine precision. These well-balanced schemes can effectively resolve small perturbations of the steady state of interest.

A wide variety of well-balanced schemes are available in the literature. Most, if not all, of them have been designed to approximate the ocean at rest steady state that arises in the shallow water equations with non-trivial bottom topography. A very limited list of such references includes [8–15] and other references therein. The design of well-balanced schemes that preserved a discrete version of some hydrostatic steady states in the Euler equations with gravitation was presented in [16,4–6] for finite volumes and in [17] for finite differences. Magnetohydrostatic steady state preserving well-balanced finite volume schemes were presented in [5].

The key principle underlying the design of most of the aforementioned well-balanced schemes consisted of replacing the piece-wise constant cell averages, used as inputs to finite volume schemes, with values constructed from a *local discrete hydrostatic equilibrium*. This results in a first-order scheme. The design of a second-order scheme requires using a well-balanced piece-wise linear reconstruction with respect of the local discrete hydrostatic equilibrium.

1.4. Scope and contents of the paper

In this paper, we design well-balanced first- and second-order accurate finite volume schemes for approximating the Euler equations with gravitation (1.1). The novel features of this paper are

- We use the equilibrium (1.11) for the construction of our well-balanced scheme. Hence, *no analytical* or *numerical integration* is necessary to perform the well-balancing equilibrium reconstruction.
- The schemes are well-balanced for *any consistent* numerical flux. This allows them to be readily implemented within any standard finite volume algorithm.
- Since the hydrostatic reconstruction is based on a fundamental thermodynamic potential, the enthalpy, it is applicable beyond the ideal gas equation of state. This is particularly important for astrophysical applications such as, e.g., core-collapse supernova explosions.
- The schemes are well-balanced with respect to multi-dimensional equilibria.
- The designed schemes do not require any *explicit* form of the gravitational potentials. In particular, the case of self-gravity is treated.

The main ingredient in our construction is the novel observation that a large class of stable hydrostatic equilibria amounts to local conditions for the enthalpy (1.11). We use this local equilibrium for the enthalpy to reconstruct the unknowns that when combined with a suitable numerical flux for the Euler equations, results in a well-balanced scheme. A suite of numerical test cases is presented to illustrate the robustness of the method. This includes the simulation of a self-gravitating model star.

The rest of the paper is organized as follows: the well-balanced finite volume schemes are presented in Section 2. Numerical results are presented in Section 3 and a summary of the paper is provided in Section 4.

2. Numerical methods

First, we will consider the Euler equations with gravitation (1.1)–(1.3) in one space dimension and write it as a balance law of the form:

$$\frac{\partial \boldsymbol{u}}{\partial t} + \frac{\partial \boldsymbol{F}}{\partial x} = \boldsymbol{S} \tag{2.1}$$

with

$$\boldsymbol{u} = \begin{bmatrix} \rho \\ \rho v_x \\ E \end{bmatrix}, \qquad \boldsymbol{F} = \begin{bmatrix} \rho v_x \\ \rho v_x^2 + p \\ (E + p)v_x \end{bmatrix} \quad \text{and} \quad \boldsymbol{S} = \begin{bmatrix} 0 \\ -\rho \\ -\rho v_x \end{bmatrix} \frac{\partial \phi}{\partial x}, \tag{2.2}$$

where $\boldsymbol{u}$, $\boldsymbol{F}$ and $\boldsymbol{S}$ are the vectors of conserved variables, fluxes and source terms. Further, we will denote the primitive variables by $\boldsymbol{w} = [\rho, v_x, p]^T$. For simplicity of presentation, we assume an ideal gas law for the equation of state:

$$p = \rho e(\gamma - 1), \tag{2.3}$$

where p is the pressure and γ is the ratio of specific heats. We note that the well-balanced schemes derived below are not tied to the choice of this particular equation of state.

The spatial domain is discretized into cells or finite volumes $I_i = [x_{i-1/2}, x_{i+1/2}]$ of uniform size $\Delta x = x_{i+1/2} - x_{i-1/2}$ (for the sake of simplicity) and the temporal domain $[0, T]$ is discretized into time steps $\Delta t^n = t^{n+1} - t^n$ where the superscript n labels the different time levels.

2.1. First-order schemes

A standard first-order finite volume scheme for approximating (2.1) is obtained by integrating (2.1) over a cell I_i and a time interval Δt^n (see e.g. [18,2,19])

$$\boldsymbol{u}_i^{n+1} = \boldsymbol{u}_i^n - \frac{\Delta t}{\Delta x}\big(\boldsymbol{F}_{i+1/2}^n - \boldsymbol{F}_{i-1/2}^n\big) + \Delta t \boldsymbol{S}_i^n, \tag{2.4}$$

where the time step has to fulfill a certain CFL condition. Here $\boldsymbol{u}_i^n$ and $\boldsymbol{u}_i^{n+1}$ are the cell averages of the conserved variables at their respective time level. The $\boldsymbol{F}_{i\pm1/2}^n$ are the numerical fluxes and $\boldsymbol{S}_i^n$ is the discretized source term to be given explicitly in the following subsections.

The numerical flux is obtained by the (approximate) solution of Riemann problems at the cell interfaces

$$\boldsymbol{F}_{i+1/2}^n = \mathcal{F}\big(\boldsymbol{w}_{i+1/2-}^n, \boldsymbol{w}_{i+1/2+}^n\big), \tag{2.5}$$

where the $\boldsymbol{w}_{i+1/2-}^n$ and $\boldsymbol{w}_{i+1/2+}^n$ are the cell interface extrapolated primitive variables, obtained from a piece-wise constant reconstruction at time t^n

$$\boldsymbol{w}_i^n(x) = \boldsymbol{w}_i^n, \quad x \in I_i, \tag{2.6}$$

and $\mathcal{F}$ is a consistent, i.e. $\mathcal{F}(\boldsymbol{w}, \boldsymbol{w}) = \boldsymbol{F}(\boldsymbol{w})$, and Lipschitz continuous numerical flux function. Below, we will make use of the HLLC approximate Riemann solver with simple wave speed estimates [19,20]. However, the here designed schemes and their equilibrium preserving properties are independent of this choice.

2.2. Well-balanced local hydrostatic reconstruction and source term discretization

As mentioned in the introduction, the standard finite volume scheme (2.4) may not exactly preserve any discrete versions of the hydrostatic equilibrium. Our aim is to design a finite volume scheme that preserves a discrete version of the hydrostatic equilibrium. To do so, we need the following two ingredients:

2.2.1. Local hydrostatic reconstruction

Within the i-th cell, we can define a subcell equilibrium reconstruction of the enthalpy by assuming (1.11) as

$$h_{0,i}^n(x) = h_i^n + \phi_i - \phi(x). \tag{2.7}$$

It remains to evaluate the gravitational potential at the cell interfaces. If the potential is any given function, then $\phi(x_{i+1/2})$ can be directly evaluated and one obtains an *exact* interface equilibrium enthalpy.

However, if the gravitational potential is only known discretely, e.g. at cell centers because it is itself obtained numerically (for instance by the numerical solution of the underlying Poisson's equation in the case of self-gravity), an interpolation procedure is needed. Note that the gravitational potential is generally a continuous (or even more regular) function and hence it has to be interpolated continuously to the cell interfaces. Therefore we use a piece-wise linear reconstruction over the staggered cells $I_{i+1/2} = [x_i, x_{i+1}]$

$$\phi(x) = \frac{1}{2}(\phi_i + \phi_{i+1}) + \frac{\phi_{i+1} - \phi_i}{\Delta x}(x - x_{i+1/2}), \quad x \in I_{i+1/2}, \tag{2.8}$$

which gives a second-order accurate representation of the gravitational potential.

Given the equilibrium enthalpy subcell distribution and assuming a constant entropy s_i within the i-th cell and the fact that the enthalpy $h = h(s, p)$, we can recover the pressure through the equation of state:

$$h_{0,i}(x) = h(s_i, p_{0,i}(x)), \quad x \in I_i. \tag{2.9}$$

The computational complexity of this inversion (solution of a non-linear algebraic equation in each cell) depends strongly on the functional form of the equation of state, but it is alleviated by the fact that we have at disposal the cell center values as good initial guesses. However, for the ideal gas law adopted here, an explicit expression can be given. We write the ideal gas law in the polytropic form

$$p = p(K, \rho) = K\rho^\gamma, \tag{2.10}$$

where K is a function of entropy alone $K = K(s)$. With (2.3), (1.9) and (2.10) one finds the subcell equilibrium reconstruction of the pressure as a function of enthalpy and K

$$p_{0,i}^n(x) = \left(\frac{1}{K_i^n}\right)^{\frac{1}{\gamma-1}} \left(\frac{\gamma-1}{\gamma} h_{0,i}^n(x)\right)^{\frac{\gamma}{\gamma-1}}. \tag{2.11}$$

Since we assume isentropic conditions within the cell, K can be simply evaluated by $K_i^n = p_i^n/(\rho_i^n)^\gamma$. In a similar fashion, one finds that the subcell equilibrium reconstruction of the density is given by

$$\rho_{0,i}^n(x) = \left(\frac{1}{K_i^n} \frac{\gamma-1}{\gamma} h_{0,i}^n(x)\right)^{\frac{1}{\gamma-1}}. \tag{2.12}$$

Given the hydrostatic reconstruction of the pressure and the density, we need to evaluate the point values of the primitive variables at cell interfaces as

$$\boldsymbol{w}_{i-1/2+}^n = \begin{bmatrix} \rho_{0,i}^n(x_{i-1/2}) \\ v_{x,i}^n \\ p_{0,i}^n(x_{i-1/2}) \end{bmatrix} \quad \text{and} \quad \boldsymbol{w}_{i+1/2-}^n = \begin{bmatrix} \rho_{0,i}^n(x_{i+1/2}) \\ v_{x,i}^n \\ p_{0,i}^n(x_{i+1/2}) \end{bmatrix}. \tag{2.13}$$

These values in turn are used in the expression for the numerical flux in the finite volume scheme (2.5). Note that the velocity is extrapolated piece-wise constantly.

2.2.2. Discretization of the source term

For the momentum source term discretization, we follow the approach suggested in [10] for the shallow water equations with topography, [4] for hydrodynamics and [5] for magnetohydrodynamics, and define

$$S_{\rho v,i}^n = \frac{p_{0,i}^n(x_{i+1/2}) - p_{0,i}^n(x_{i-1/2})}{\Delta x}, \tag{2.14}$$

where $p_{0,i}^n(x_{i\pm1/2})$ is given by (2.11).

For the discretization of the energy source term, we use the second-order spatially accurate expression:

$$S_{E,i}^n = -\rho v_{x,i}^n \frac{\phi_{i+1} - \phi_{i-1}}{2\Delta x} = -\int_{x_{i-1/2}}^{x_{i+1/2}} \rho v_x \frac{\partial \phi}{\partial x}\, dx + O(\Delta x^2). \tag{2.15}$$

The above sources are combined to evaluate the source vector:

$$\boldsymbol{S}_i^n = \begin{bmatrix} 0 \\ S_{\rho v,i}^n \\ S_{E,i}^n \end{bmatrix}. \tag{2.16}$$

This completes the specification of the well-balanced scheme.

The theorem below summarizes some properties of the resulting first-order scheme:

Theorem 1. *Consider the scheme* (2.4) *approximating* (2.1) *with a consistent and Lipschitz continuous numerical flux* $\mathcal{F}$, *the hydrostatic reconstruction* (2.13) (*with* (2.11), (2.12)) *and the gravitational source term* (2.16) (*with* (2.15) *and* (2.14)).

This scheme has then the following properties:

 (i) *The scheme* (2.4) *is consistent with* (2.1) *and it is first-order accurate in time and space* (*for smooth solutions*).
(ii) *The scheme is well-balanced and preserves the discrete hydrostatic equilibrium given by* (1.11) *and* $v_x = 0$ *exactly*.

Proof. (i) The consistency of (2.4) with (2.1) is straightforward, except for the consistency of the momentum source term. From the thermodynamic relation (1.8) and the fact that we assume constant entropy within the cell, it is clear that the pressure is a function of enthalpy alone $p = p(h, s) = p(h)$. The right interface pressure $p_{0,i}^n(x_{i+1/2})$ of the i-th cell is simply obtained by evaluating it at the interface enthalpy

$$p_{0,i}^n(x_{i+1/2}) = p\big(h_{0,i}^n(x_{i+1/2})\big) = p\big(h_i^n + \phi_i - \phi(x_{i+1/2})\big) = p\big(h_i^n + \Delta h_{i+}\big),$$

where we define

$$\Delta h_{i+} = -\big(\phi(x_{i+1/2}) - \phi_i\big).$$

Assuming a smooth dependence of the pressure on the enthalpy, we can expand the pressure as

$$p\big(h_i^n + \Delta h_{i+}\big) = p\big(h_i^n\big) + \Delta h_{i+}\frac{\partial p}{\partial h}\big(h_i^n\big) + \sum_{k \geqslant 2}\frac{\Delta h_{i+}^k}{k!}\frac{\partial^k p}{\partial h^k}\big(h_i^n\big) = p_i^n + \Delta h_{i+}\rho_i^n + \sum_{k \geqslant 2}\frac{\Delta h_{i+}^k}{k!}\frac{\partial^k p}{\partial h^k}\big(h_i^n\big),$$

where we used the thermodynamic relation (1.8) in the second term. In the same fashion, we can expand the left interface pressure $p_{0,i}^n(x_{i-1/2})$ of the i-th cell to

$$p\big(h_i^n - \Delta h_{i-}\big) = p\big(h_i^n\big) - \Delta h_{i-}\frac{\partial p}{\partial h}\big(h_i^n\big) + \sum_{k \geqslant 2}(-1)^k\frac{\Delta h_{i-}^k}{k!}\frac{\partial^k p}{\partial h^k}\big(h_i^n\big) = p_i^n - \Delta h_{i-}\rho_i^n + \sum_{k \geqslant 2}(-1)^k\frac{\Delta h_{i-}^k}{k!}\frac{\partial^k p}{\partial h^k}\big(h_i^n\big),$$

where we define

$$\Delta h_{i-} = -\big(\phi_i - \phi(x_{i-1/2})\big).$$

The momentum source term (2.14) then becomes

$$\begin{aligned}
S_{\rho v,i}^n &= \rho_i^n\frac{\Delta h_{i+} + \Delta h_{i-}}{\Delta x} + \frac{1}{\Delta x}\sum_{k \geqslant 2}\frac{1}{k!}\big(\Delta h_{i+}^k - (-1)^k\Delta h_{i-}^k\big)\frac{\partial^k p}{\partial h^k}\big(h_i^n\big) \\
&= -\rho_i^n\frac{\phi(x_{i+1/2}) - \phi(x_{i-1/2})}{\Delta x} + \frac{1}{\Delta x}\sum_{k \geqslant 2}\frac{1}{k!}\big(\Delta h_{i+}^k - (-1)^k\Delta h_{i-}^k\big)\frac{\partial^k p}{\partial h^k}\big(h_i^n\big) \\
&= -\rho_i^n\frac{\phi_{i+1} - \phi_{i-1}}{\Delta x} + \frac{1}{\Delta x}\sum_{k \geqslant 2}\frac{1}{k!}\big(\Delta h_{i+}^k - (-1)^k\Delta h_{i-}^k\big)\frac{\partial^k p}{\partial h^k}\big(h_i^n\big) \\
&= -\int_{x_{i-1/2}}^{x_{i+1/2}}\rho\frac{\partial\phi}{\partial x}\mathrm{d}x + O\big(\Delta x^2\big).
\end{aligned}$$

In the second equality the definitions of the $\Delta h_{i\pm}$ were used and in the third equality the linear interpolation of the gravitational potential (2.8) was substituted. The first term on the second and third lines are clearly second-order accurate discretizations of the momentum source term (even if the gravitational potential can be explicitly evaluated at the interface). However, the second term is also of order $O(\Delta x^2)$ and this is demonstrated in Appendix A. Thus we showed the consistency of the well-balanced momentum source term discretization. Moreover, we showed that it is actually a second-order approximation.

The proof of the formal order of accuracy is straightforward as the hydrostatic reconstruction of the density and the pressure and the discretized momentum source term are second-order accurate whereas the velocity input to the numerical flux and the forward Euler time stepping are first-order accurate, resulting in an overall first-order of accuracy.

(ii) To prove the well-balancing, insert data satisfying (1.11) into (2.7) to obtain $h_{i+1/2-}^n = h_{i+1/2+}^n = h_{i+1/2}^n$. With (2.11) and (2.12) one obtains $p_{i+1/2-}^n = p_{i+1/2+}^n = p_{i+1/2}^n$ and $\rho_{i+1/2-}^n = \rho_{i+1/2+}^n = \rho_{i+1/2}^n$. Plugging the later result and $v_{x,i} = 0$ into a consistent numerical flux yields

$$\boldsymbol{F}_{i+1/2}^n = \mathcal{F}\big([\rho_{i+1/2}^n, 0, p_{i+1/2}^n]^T, [\rho_{i+1/2}^n, 0, p_{i+1/2}^n]^T\big) = \begin{bmatrix} 0 \\ p_{i+1/2}^n \\ 0 \end{bmatrix}.$$

In the same way, we can evaluate the gravitational source term (2.16) with (2.14) and (2.15) to obtain

$$\boldsymbol{S}_i^n = \begin{bmatrix} 0 \\ \frac{p_{i+1/2}^n - p_{i-1/2}^n}{\Delta x} \\ 0 \end{bmatrix}.$$

Combining the above expressions for the numerical flux and source term one obtains

$$\frac{\boldsymbol{F}_{i+1/2}^n - \boldsymbol{F}_{i-1/2}^n}{\Delta x} = \boldsymbol{S}_i^n,$$

showing the well-balanced property of the scheme. $\quad\square$

2.3. Second-order schemes

Due to the limited practical use of first-order schemes, a higher order extension is needed. Hence, we will design a well-balanced second-order accurate (in both space and time) finite volume scheme in the following.

A semi-discrete scheme for (2.1) may be written as

$$\frac{\mathrm{d}\boldsymbol{u}_i}{\mathrm{d}t} = \boldsymbol{L}(\boldsymbol{u}) = -\frac{1}{\Delta x}(\boldsymbol{F}_{i+1/2} - \boldsymbol{F}_{i-1/2}) + \boldsymbol{S}_i, \tag{2.17}$$

where $\boldsymbol{F}_{i\pm1/2}$ is the numerical flux through $x_{i\pm1/2}$ and $\boldsymbol{S}_i$ is the gravity source term.

In order to increase the spatial resolution, the piece-wise constant reconstruction of the cell interface values $\boldsymbol{w}_{i+1/2}^-$ and $\boldsymbol{w}_{i+1/2}^+$, input to the numerical flux $\boldsymbol{F}_{i+1/2} = \mathcal{F}(\boldsymbol{w}_{i+1/2}^-, \boldsymbol{w}_{i+1/2}^+)$, is replaced by a higher order non-oscillatory reconstruction $\boldsymbol{w}_i(x)$, see e.g. [18,2,19]. Several reconstruction methods are available including the TVD-MUSCL [21], ENO [22] and WENO reconstructions [23].

2.3.1. Second-order equilibrium preserving reconstruction

A standard piece-wise linear reconstruction for some state variable q is given by

$$q_i(x) = q_i + Dq_i(x - x_i), \quad x \in I_i, \tag{2.18}$$

where Dq_i denotes a (limited) slope. One simple choice for the slope is given by the so-called *minmod* limiter,

$$Dq_i = \mathrm{minmod}\left(\frac{q_i - q_{i-1}}{\Delta x}, \frac{q_{i+1} - q_i}{\Delta x}\right), \tag{2.19}$$

where

$$\mathrm{minmod}(a, b) = \frac{1}{2}\big(\mathrm{sign}(a) + \mathrm{sign}(b)\big)\min\big(|a|, |b|\big). \tag{2.20}$$

The cell interface values of the state variable q are then simply given by

$$q_{i-1/2+} = q_i(x_{i-1/2}) \quad \text{and} \quad q_{i+1/2-} = q_i(x_{i+1/2}). \tag{2.21}$$

Applying the standard reconstruction (2.18) and (2.19) to density ρ, velocity v_x and pressure p results in second-order accurate interface values (2.21).

A straightforward reconstruction of pressure and density, as outlined above, does not preserve a discrete hydrostatic equilibrium. To design an equilibrium preserving reconstruction within the i-th cell $q_i(x)$, we decompose the sought for reconstruction into an equilibrium $q_{0,i}(x)$ and a perturbation $q_{1,i}(x)$. Here q stands for either pressure or density. The equilibrium reconstructions are given by (2.11) for the pressure and (2.12) for the density.

For the perturbation we then apply a standard piece-wise linear reconstruction

$$q_{1,i}(x) = q_{1,i}(x_i) + Dq_{1,i}(x - x_i), \quad x \in I_i. \tag{2.22}$$

The data for the reconstruction of the perturbation $q_{1,i}(x)$ are obtained by extrapolating the equilibrium reconstruction of the i-th cell to the neighboring cells $i-1$ and $i+1$:

$$q_{1,i}(x_{i-1}) = q_{i-1} - q_{0,i}(x_{i-1}), \qquad q_{1,i}(x_{i+1}) = q_{i+1} - q_{0,i}(x_{i+1}).$$

Note that $q_{1,i}(x_i) = q_i - q_{0,i}(x_i) = 0$ holds, i.e. the equilibrium reconstruction equals the cell average q_i at the cell center. The limited slope of the perturbation reconstruction can then be computed by

$$Dq_{1,i} = \mathrm{minmod}\left(\frac{q_{1,i}(x_i) - q_{1,i}(x_{i-1})}{\Delta x}, \frac{q_{1,i}(x_{i+1}) - q_{1,i}(x_i)}{\Delta x}\right). \tag{2.23}$$

Finally, the equilibrium preserving second-order accurate reconstruction within the i-th cell $q_i(x)$ is given by

$$q_i(x) = q_{0,i}(x) + q_{1,i}(x), \quad x \in I_i. \tag{2.24}$$

For the sake of clarity, the equilibrium preserving reconstruction is schematized in Fig. 1. Note that if we are given a hydrostatic equilibrium, then the reconstruction preserves the equilibrium exactly since in this case the perturbation vanishes by design, i.e. $q_{1,i}(x) = 0$.

In summary, the second-order well-balanced schemes are given by a local hydrostatic subcell reconstruction,

$$\boldsymbol{w}_{i-1/2+} = \begin{bmatrix} \rho_{0,i}(x_{i-1/2}) + \rho_{1,i}(x_{i-1/2}) \\ v_{x,i}(x_{i-1/2}) \\ p_{0,i}(x_{i-1/2}) + p_{1,i}(x_{i-1/2}) \end{bmatrix} \quad \text{and} \quad \boldsymbol{w}_{i+1/2-} = \begin{bmatrix} \rho_{0,i}(x_{i+1/2}) + \rho_{1,i}(x_{i+1/2}) \\ v_{x,i}(x_{i+1/2}) \\ p_{0,i}(x_{i+1/2}) + p_{1,i}(x_{i+1/2}) \end{bmatrix}, \tag{2.25}$$
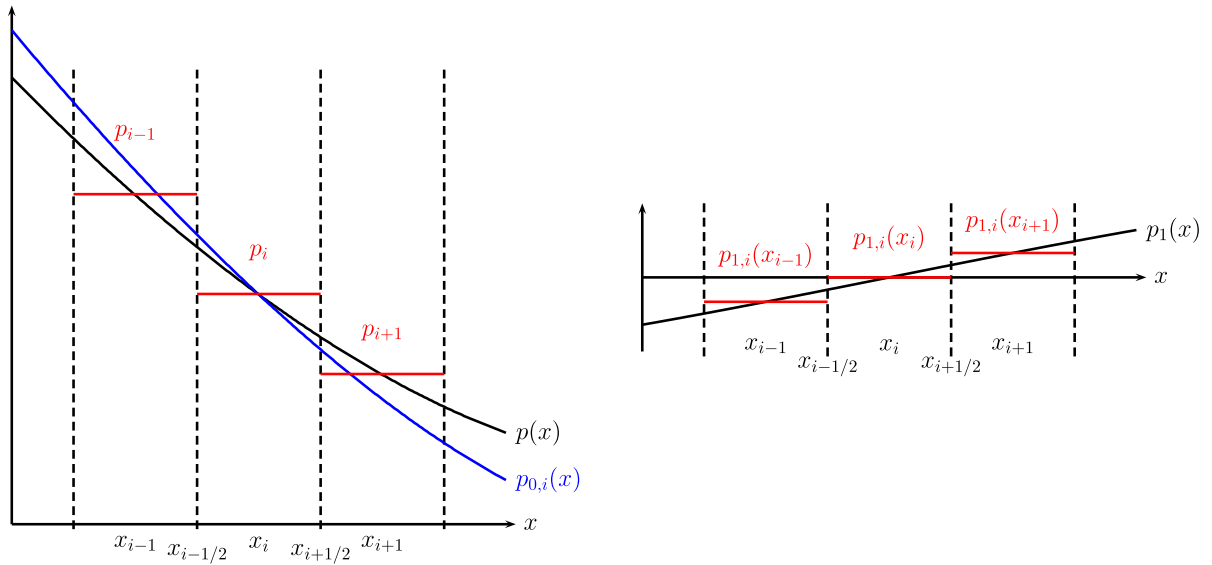
Fig. 1. Sketch of the equilibrium preserving reconstruction of the pressure. Left panel: At the beginning of the reconstruction process, we are given the cell averages of the i-th cell and its immediate neighbors (red lines). We seek to approximate the exact distribution of the pressure $p(x)$ (black line) by a piece-wise linear equilibrium preserving reconstruction $p_i(x)$. This is achieved by extrapolating the equilibrium distribution within the i-th cell $p_{0,i}(x)$ (blue line) to the neighboring cells and computing the perturbation at the respective cell centers. Right: Now we can apply a standard piece-wise linear reconstruction to the perturbation cell averages $p_{1,i}(x_{i-1})$, $p_{1,i}(x_i)$ and $p_{1,i}(x_{i+1})$ (red lines). This will result in a second-order approximation of the exact pressure perturbation distribution. (For interpretation of the references to color in this figure legend, the reader is referred to the web version of this article.)

and the momentum source discretization

$$S^n_{\rho v, i} = \frac{p_{0,i}(x_{i+1/2}) - p_{0,i}(x_{i-1/2})}{\Delta x}. \tag{2.26}$$

Here the equilibrium density $\rho_{0,i}(x)$ and pressure $p_{0,i}(x)$ reconstructions are obtained by the procedure described in Section 2.2. The density $\rho_{1,i}(x)$ and pressure $p_{1,i}(x)$ perturbations are computed with the equilibrium preserving piece-wise linear reconstruction (2.22) and (2.23). The interface velocity is obtained by a standard piece-wise linear reconstruction (2.18) and (2.19).

2.3.2. Time stepping

For second-order accurate integration in time, we use the second-order strong stability preserving (SSP) Runge–Kutta time stepping (see [24])

$$\boldsymbol{u}_i^* = \boldsymbol{u}_i + \Delta t^n \boldsymbol{L}(\boldsymbol{u}^n), \qquad \boldsymbol{u}_i^{**} = \boldsymbol{u}_i^* + \Delta t^n \boldsymbol{L}(\boldsymbol{u}^*), \qquad \boldsymbol{u}_i^{n+1} = \frac{1}{2}(\boldsymbol{u}_i^* + \boldsymbol{u}_i^{**}), \tag{2.27}$$

where $\boldsymbol{L}$ is defined in (2.17) and the time step Δt^n is determined by a suitable CFL condition.

We then have the following result for the second-order scheme:

Corollary 2. *The well-balanced scheme for hydrostatic equilibrium described in Theorem 1 becomes second-order accurate in time and space with the equilibrium reconstruction (2.25) (for smooth solutions).*

Proof. At equilibrium, the perturbations are zero and the scheme reduces to the previous scheme and thus is exactly well-balanced. The proof of accuracy is a straightforward consequence of the second-order reconstruction being used as inputs for the numerical flux and second-order discretization of the momentum and energy source terms.

2.4. Extension to several space dimensions

We now discuss the extension of our well-balanced scheme for hydrostatic equilibrium to the multi-dimensional case. For convenience we describe it for two dimensions and the extension to three dimensions is analogous.

The two-dimensional Euler equations with gravity in Cartesian coordinates are given by

$$\frac{\partial \boldsymbol{u}}{\partial t} + \frac{\partial \boldsymbol{F}}{\partial x} + \frac{\partial \boldsymbol{G}}{\partial y} = \boldsymbol{S} \tag{2.28}$$

with

$$
\boldsymbol{u} = \begin{bmatrix} \rho \\ \rho v_x \\ \rho v_y \\ E \end{bmatrix}, \qquad \boldsymbol{F} = \begin{bmatrix} \rho v_x \\ \rho v_x^2 + p \\ \rho v_y v_x \\ (E+p) v_x \end{bmatrix},
$$

$$
\boldsymbol{G} = \begin{bmatrix} \rho v_y \\ \rho v_x v_y \\ \rho v_y^2 + p \\ (E+p) v_y \end{bmatrix} \quad \text{and} \quad \boldsymbol{S} = \boldsymbol{S}_x + \boldsymbol{S}_y = \begin{bmatrix} 0 \\ -\rho \\ 0 \\ -\rho v_x \end{bmatrix} \frac{\partial \phi}{\partial x} + \begin{bmatrix} 0 \\ 0 \\ -\rho \\ -\rho v_y \end{bmatrix} \frac{\partial \phi}{\partial y}. \tag{2.29}
$$

The primitive variables are given by $\boldsymbol{w} = [\rho, v_x, v_y, p]^T$.

We discretize space into cells or finite volumes $I_{i,j} = [x_{i-1/2}, x_{i+1/2}] \times [y_{j-1/2}, y_{j+1/2}]$ of uniform size $\Delta x = x_{i+1/2} - x_{i-1/2}$ and $\Delta y = y_{j+1/2} - y_{j-1/2}$. By integrating (2.28) over a cell $I_{i,j}$ we obtain a semi-discrete scheme for the evolution of the cell averaged conserved quantities $\boldsymbol{u}_{i,j}$

$$
\frac{d\boldsymbol{u}_{i,j}}{dt} = \boldsymbol{L}(\boldsymbol{u}) = -\frac{1}{\Delta x}(\boldsymbol{F}_{i+1/2,j} - \boldsymbol{F}_{i-1/2,j}) - \frac{1}{\Delta y}(\boldsymbol{G}_{i,j+1/2} - \boldsymbol{G}_{i,j-1/2}) + \boldsymbol{S}_{i,j}, \tag{2.30}
$$

where $\boldsymbol{F}_{i+1/2,j} = \mathcal{F}(\boldsymbol{w}_{i+1/2-,j}, \boldsymbol{w}_{i+1/2+,j})$ and $\boldsymbol{G}_{i,j+1/2} = \mathcal{G}(\boldsymbol{w}_{i,j+1/2-}, \boldsymbol{w}_{i,j+1/2+})$ are the numerical fluxes in the respective direction and $\boldsymbol{S}_{i,j}$ is the gravity source term. The $\boldsymbol{w}_{i+1/2\pm,j}$ and $\boldsymbol{w}_{i,j+1/2\pm}$ are the cell interface extrapolated primitive variables.

In analogy with the one-dimensional schemes, our first-order two-dimensional well-balanced scheme for hydrostatic equilibrium consists of two ingredients: (1) local hydrostatic subcell reconstructions of the pressure $p_{0,i,j}(x, y)$ and the density $\rho_{0,i,j}(x, y)$, which are then used to recover the cell interface primitive variables

$$
\boldsymbol{w}_{i\mp 1/2\pm,j} = \begin{bmatrix} \rho_{0,i,j}(x_{i\mp 1/2}, y_j) \\ v_{x,i,j} \\ v_{y,i,j} \\ p_{0,i}(x_{i\mp 1/2}, y_j) \end{bmatrix} \quad \text{and} \quad \boldsymbol{w}_{i,j\mp 1/2\pm} = \begin{bmatrix} \rho_{0,i,j}(x_i, y_{j\mp 1/2}) \\ v_{x,i,j} \\ v_{y,i,j} \\ p_{0,i,j}(x_i, y_{j\mp 1/2}) \end{bmatrix}, \tag{2.31}
$$

and (2) a well-balanced discretization of the gravitational source term

$$
\boldsymbol{S}_{x,i,j} = \begin{bmatrix} 0 \\ S_{x,\rho v,i,j} \\ 0 \\ S_{x,E,i,j} \end{bmatrix} \quad \text{and} \quad \boldsymbol{S}_{y,i,j} = \begin{bmatrix} 0 \\ 0 \\ S_{y,\rho v,i,j} \\ S_{y,E,i,j} \end{bmatrix}. \tag{2.32}
$$

Since we are here only concerned with the hydrostatic state, we use the following standard centered discretization for the energy source terms

$$
S_{x,E,i} = -\rho v_{x,i,j} \frac{\phi_{i+1,j} - \phi_{i-1,j}}{2\Delta x} \quad \text{and} \quad S_{y,E,i} = -\rho v_{y,i,j} \frac{\phi_{i,j+1} - \phi_{i,j-1}}{2\Delta y}, \tag{2.33}
$$

which are spatially second-order accurate.

The equilibrium (1.11) is indeed also valid in the multi-dimensional case. Therefore we can define a two-dimensional subcell equilibrium reconstruction of the enthalpy in a straightforward manner by

$$
h_{0,i,j}(x, y) = h_{i,j} + \phi_{i,j} - \phi(x, y), \quad (x, y) \in I_{i,j}. \tag{2.34}
$$

Here again it remains to evaluate the gravitational potential. If the potential is a known function, then $\phi(x, y)$ can be directly evaluated and one obtains an exact subcell hydrostatic reconstruction of the enthalpy.

However, if the gravitational potential is only known discretely, we need a continuous interpolation. To achieve this, we use a piece-wise *bilinear* reconstruction over the staggered cell $I_{i+1/2,j+1/2} = [x_i, x_{i+1}] \times [y_j, y_{j+1}]$

$$
\begin{aligned}
\phi(x, y) &= \frac{1}{4}(\phi_{i,j} + \phi_{i+1,j} + \phi_{i,j+1} + \phi_{i+1,j+1}) + \frac{\frac{1}{2}(\phi_{i+1,j} + \phi_{i+1,j+1}) - \frac{1}{2}(\phi_{i,j} + \phi_{i,j+1})}{\Delta x}(x - x_{i+1/2}) \\
&\quad + \frac{\frac{1}{2}(\phi_{i,j+1} + \phi_{i+1,j+1}) - \frac{1}{2}(\phi_{i,j} + \phi_{i+1,j})}{\Delta y}(y - y_{j+1/2}), \quad (x, y) \in I_{i+1/2,j+1/2},
\end{aligned} \tag{2.35}
$$

which results in a second-order accurate representation of the gravitational field. With the subcell equilibrium reconstruction of the enthalpy we can derive, as in the one-dimensional case, the equilibrium pressure

$$
p_{0,i}(x, y) = \left(\frac{1}{K_{i,j}}\right)^{\frac{1}{\gamma-1}} \left(\frac{\gamma-1}{\gamma} h_{0,i,j}(x, y)\right)^{\frac{\gamma}{\gamma-1}} \tag{2.36}
$$

and density

$$\rho_{0,i,j}(x,y) = \left(\frac{1}{K_{i,j}} \frac{\gamma-1}{\gamma} h_{0,i,j}(x,y) \right)^{\frac{1}{\gamma-1}} \tag{2.37}$$

distributions. Here $K_{i,j} = p_{i,j}/\rho_{i,j}^{\gamma}$ is evaluated as in the one-dimensional setting. With (2.36) and (2.37) we obtain the cell interface primitive variables (2.31).

The momentum source terms are discretized on a dimension-by-dimension basis

$$S_{x,\rho v,i,j} = \frac{p_{0,i,j}(x_{i+1/2}, y_j) - p_{0,i,j}(x_{i-1/2}, y_j)}{\Delta x} \quad \text{and} \quad S_{y,\rho v,i,j} = \frac{p_{0,i,j}(x_i, y_{j+1/2}) - p_{0,i,j}(x_i, y_{j-1/2})}{\Delta y}, \tag{2.38}$$

which completes the specification of the gravitational source term (2.32).

The reconstruction (2.31) is only first-order accurate away from equilibrium. Second-order accuracy is obtained by applying the equilibrium preserving piece-wise linear reconstruction described in Section 2.3 to the pressure and the density in a dimension-by-dimension manner. A standard piece-wise linear reconstruction is applied to the velocity. The second-order accurate interface primitive variables are then given by

$$\boldsymbol{w}_{i\mp1/2\pm,j} = \begin{bmatrix} \rho_{0,i,j}(x_{i\mp1/2}, y_j) + \rho_{1,i,j}(x_{i\mp1/2}, y_j) \\ v_{x,i,j}(x_{i\mp1/2}, y_j) \\ v_{y,i,j}(x_{i\mp1/2}, y_j) \\ p_{0,i,j}(x_{i\mp1/2}, y_j) + p_{1,i}(x_{i\mp1/2}, y_j) \end{bmatrix} \quad \text{and}$$

$$\boldsymbol{w}_{i,j\mp1/2\pm} = \begin{bmatrix} \rho_{0,i,j}(x_i, y_{j\mp1/2}) + \rho_{1,i,j}(x_i, y_{j\mp1/2}) \\ v_{x,i,j}(x_i, y_{j\mp1/2}) \\ v_{y,i,j}(x_i, y_{j\mp1/2}) \\ p_{0,i,j}(x_i, y_{j\mp1/2}) + p_{1,i,j}(x_i, y_{j\mp1/2}) \end{bmatrix}. \tag{2.39}$$

A fully discrete second-order accurate scheme is obtained by the SSP Runge–Kutta time stepping (2.27). This completes the description of the two-dimensional well-balanced scheme for hydrostatic equilibrium and its properties are summarized in the corollary below:

Corollary 3. *Consider the scheme* (2.30) *approximating* (2.28) *with a consistent and Lipschitz continuous numerical flux, the hydrostatic reconstruction* (2.39) *(with* (2.36), (2.37)*), the gravitational source term* (2.32) *(with* (2.33) *and* (2.38)*) and the time stepping* (2.27).

This scheme has then the following properties:

 (i) *The scheme* (2.30) *is consistent with* (2.28) *and it is second-order accurate in time and space* (*for smooth solutions*).
(ii) *The scheme is well-balanced and preserves a second-order accurate discrete hydrostatic equilibrium given by* (1.11) *and* $v_x = 0$ *exactly.*

Proof. The proof follows directly by applying Theorem 1 dimension-by-dimension. ∎

3. Numerical results

In this section we test our well-balanced schemes (designed in the previous section) on a series of numerical experiments. For comparison, we also consider unbalanced base schemes by switching off the hydrostatic reconstruction and using a standard centered discretization of the momentum source term, i.e. in the one-dimensional case

$$S_{\rho v,i} = -\rho_i \frac{\phi_{i+1} - \phi_{i-1}}{2\Delta x}. \tag{3.1}$$

To characterize a time scale on which a model reacts to perturbations of its equilibrium, we define the sound crossing time τ_{sound}

$$\tau_{\text{sound}} = 2 \int\limits_{x_0}^{x_1} \frac{dx}{c}, \tag{3.2}$$

where $c = (\gamma p/\rho)^{1/2}$ is the speed of sound and the integral has to be taken over the extent of the stationary state of interest.

We quantify the accuracy of the schemes by computing the errors

$$Err = \left\| q_i - q_i^{\text{ref}} \right\|_1 \tag{3.3}$$

where $\|.\|_1$ denotes the 1-norm. Here q is a selected relevant quantity (e.g. density, pressure, …) and q^{ref} is a reference solution, i.e. the stationary state to be maintained discretely or an interpolated numerically obtained reference solution on very fine grid. While the comparison with a numerically obtained reference solution does not provide a rigorous evidence of convergence, it nevertheless indicates a meaningful measure of the errors.

3.1. One-dimensional results: Hydrostatic atmosphere in a constant gravitational field

We consider the very simple setting of an isentropic hydrostatic atmosphere in a constant gravitational field. The gravitational potential is then a simple linear function

$$\phi(x) = gx, \tag{3.4}$$

where g is the constant gravitational acceleration. In practice, problems of similar type arise for example in numerical weather prediction [4] and in the simulation of wave propagation in stellar atmospheres [5].

The density and pressure profiles are then given by

$$\rho(x) = \left(\rho_0^{\gamma-1} - K_0 \frac{\gamma-1}{\gamma} gx\right)^{\frac{1}{\gamma-1}} \quad \text{and} \quad p(x) = K_0 \rho(x)^\gamma, \tag{3.5}$$

with the constants $g = 1$, $\gamma = 5/3$, $\rho_0 = 1$, $p_0 = 1$ and $K_0 = p_0/\rho_0^\gamma$. The computational domain is set to $x \in [0, L]$ with $L = 2$ and discretized by N cells, i.e. we set $\Delta x = L/N$, $x_{i+1/2} = i\Delta x$ and $x_i = (x_{i-1/2} + x_{i+1/2})/2$ with $i = 1, \ldots, N$. The velocity is set to zero everywhere.

The boundaries are treated as follows. For the first-order schemes, we specify one ghost cell on either end by simply extrapolating the hydrostatic reconstruction of density and pressure from the last physical cell

$$\rho_0 = \rho_{0,1}(x_0), \qquad \rho_{N+1} = \rho_{0,N}(x_{N+1}), \qquad p_0 = p_{0,1}(x_0), \qquad p_{N+1} = p_{0,N}(x_{N+1}). \tag{3.6}$$

For the velocity we use a simple zero-order extrapolation

$$v_{x,0} = v_{x,1}, \qquad v_{x,N+1} = v_{x,N}. \tag{3.7}$$

For the second-order schemes, we specify two ghost cells. For the pressure end the density, we perform a first-order equilibrium extrapolation

$$\begin{aligned} \rho_m &= \rho_{0,1}(x_m) + \rho_{1,1}(x_m), \qquad \rho_{N-m} = \rho_{0,N}(x_{N-m}) + \rho_{1,N}(x_{N-m}), \\ p_m &= p_{0,1}(x_m) + p_{1,1}(x_m), \qquad p_{N-m} = p_{0,N}(x_{N-m}) + p_{1,N}(x_{N-1}), \end{aligned} \tag{3.8}$$

where $m \in \{1, 2\}$ and the slope of the perturbations are computed from the interior solution

$$\begin{aligned} D\rho_{1,1} &= \frac{\rho_2 - \rho_{0,1}(x_2)}{\Delta x}, \qquad D\rho_{1,N} = \frac{\rho_{0,N}(x_{N-1}) - \rho_{N-1}}{\Delta x}, \\ Dp_{1,1} &= \frac{p_2 - p_{0,1}(x_2)}{\Delta x}, \qquad Dp_{1,N} = \frac{p_{0,N}(x_{N-1}) - p_{N-1}}{\Delta x}. \end{aligned} \tag{3.9}$$

In a similar way, the velocity is extrapolated in a piece-wise-linear fashion to the ghost cells based on the interior solution.

3.1.1. Well-balanced property

We begin by numerically verifying the well-balancing properties of the schemes. To this end, we evolve the isentropic hydrostatic equilibrium atmosphere for one sound crossing time $t = 4$ ($\tau_{\mathrm{sound}} \approx 3.92$) and resolutions $N = 128, 256, 512, 1024, 2048$. The numerical errors for the pressure at final time are reported in Table 1. The table clearly shows that the first-order and second-order well-balanced schemes maintain the stationary state to machine precision. The unbalanced versions of the schemes produce large errors and are definitely not able to maintain the discrete stationary state accurately. Although their errors diminish with increasing resolution at the expected rate, they are unsuitable for the simulation of small perturbations (i.e. on the order of the truncation errors) of the hydrostatic equilibrium.

3.1.2. Small amplitude wave propagation

As a second test, we compare the ability of the well-balanced/unbalanced second-order schemes to propagate small disturbances on top of the isentropic hydrostatic atmosphere. To do so, we impose a periodic velocity perturbation at the bottom of the atmosphere

$$v_{x,m}^n = A \sin(4\pi t^n), \tag{3.10}$$

where $m \in \{-1, 0\}$. A similar setup was used in [5]. For the amplitude we set $A = 10^{-6}$ and evolve the generated waves until $t = 1.5$ (shortly before the waves reach the upper boundary). The excited waves move through the domain and are modified by the density and pressure stratification of the atmosphere.

Table 1

Error in pressure for the isentropic hydrostatic atmosphere computed with the unbalanced/well-balanced first and second-order schemes.

N	First	Second
128	2.12E–02/1.34E–14	6.46E–05/1.29E–14
256	1.06E–02/3.57E–14	1.63E–05/1.52E–14
512	5.28E–03/7.73E–14	4.09E–06/4.61E–14
1024	2.64E–03/5.69E–14	1.02E–06/6.11E–14
2048	1.32E–03/1.15E–13	2.56E–07/1.53E–14
Rate	1.00/–	2.00/–

Table 2

Error in pressure and velocity for the small amplitude waves on the isentropic hydrostatic atmosphere computed with the unbalanced/balanced second-order schemes.

N	Pressure	Velocity
128	3.12E–05/1.85E–07	1.48E–05/4.27E–07
256	7.80E–06/6.82E–08	3.67E–06/1.68E–07
512	1.95E–06/2.51E–08	9.11E–07/6.10E–08
1024	4.84E–07/8.53E–09	2.27E–07/1.90E–08
2048	1.18E–07/4.12E–09	5.66E–08/5.80E–09
Rate	2.01/1.40	2.01/1.55

(a) Pressure perturbation   (b) Velocity
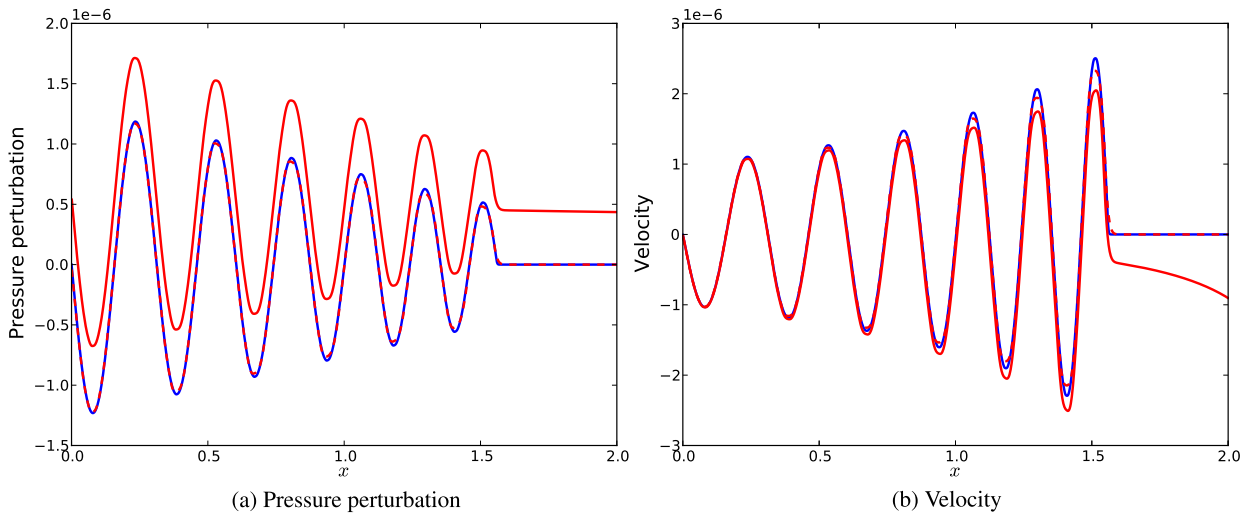
Fig. 2. Small amplitude waves traveling up the isentropic hydrostatic atmosphere. The solid blue line represents the reference solution and was obtained with the second-order well-balanced scheme and $N = 8192$ cells. The solid/dashed red line represent the solution obtained with the unbalanced/balanced second-order scheme and $N = 1024$. (For interpretation of the references to color in this figure legend, the reader is referred to the web version of this article.)

The errors in pressure and velocity with the second-order version of both schemes are displayed in Table 2. The errors were evaluated on the basis of a reference solution obtained with the well-balanced second-order scheme at high resolution $N = 8192$.

We observe that the errors with the well-balanced scheme are roughly two orders of magnitude smaller than with the unbalanced scheme. Moreover, the velocity of the unbalanced scheme are larger than the amplitude of the excited waves for $N < 512$. Hence, the unbalanced schemes are not able to resolve the wave pattern for these resolutions. The well-balanced scheme is able to resolve the waves for all resolutions.

The pressure perturbation, i.e. pressure at final time minus initial pressure profile, and the velocity profile for the unbalanced/balanced (solid/dashed red line) for $N = 1024$ together with the reference solution (solid blue line) are plotted in Fig. 2. From this figure, we observe that the unbalanced scheme produces spurious deviations. However, the well-balanced scheme captures the wave pattern very well. This underlines the fact that the well-balanced scheme is superior in capturing small perturbation of a stationary state.

Table 3
Error in pressure and velocity for the large amplitude waves on the isentropic hydrostatic atmosphere computed with the unbalanced/balanced second-order schemes.

N	Pressure	Velocity
128	9.78E–03/1.14E–02	1.74E–02/2.04E–02
256	4.14E–03/4.88E–03	7.53E–03/8.71E–03
512	1.85E–03/2.04E–03	3.75E–03/3.82E–03
1024	8.73E–04/8.00E–04	1.73E–03/1.49E–03
2048	5.53E–04/3.33E–04	1.04E–03/6.54E–04
Rate	1.05/1.28	1.02/1.25

(a) Pressure perturbation

(b) Velocity
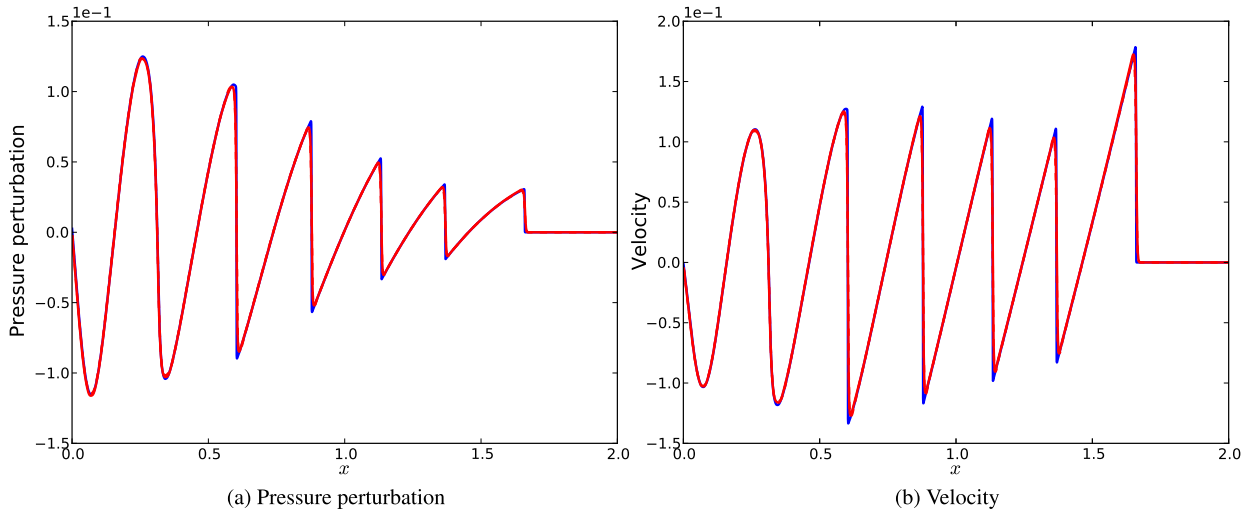
Fig. 3. Large amplitude waves traveling up the isentropic hydrostatic atmosphere. The solid blue line represents the reference solution and was obtained with the second-order well-balanced scheme and $N = 8192$ cells. The solid/dashed red line represent the solution obtained with the unbalanced/balanced second-order scheme and $N = 1024$. Note that the two solutions are indistinguishable by eye, as to be expected on the strong amplitude perturbation. (For interpretation of the references to color in this figure legend, the reader is referred to the web version of this article.)

3.1.3. Large amplitude wave propagation

In order to check that the well-balanced hydrostatic reconstruction does not destroy the robustness of the base high resolution shock capturing finite volume scheme, we repeat the previous test with large amplitude perturbations at the bottom. We set $A = 0.1$ and evolve the generated waves until $t = 1.5$ (shortly before the waves reach the upper boundary).

The errors in pressure and velocity are reported in Table 3. The errors were computed on the basis of a reference solution computed with the well-balanced scheme at high resolution $N = 8192$. Both, the unbalanced and the well-balance second-order schemes show a rate of convergence close to one and the errors are of comparable size. This is to be expected, because the sine waves steepen into saw-tooth waves while propagating up the atmosphere. This is displayed in Fig. 3. The large amplitude test illustrates that the hydrostatic reconstruction does not deteriorate the accuracy and the robustness of the base high resolution shock capturing scheme.

3.2. Three-dimensional polytrope

As a three-dimensional test, we show the performance of our hydrostatic reconstruction scheme on an astrophysical problem. We simulate a static configuration of an adiabatic gaseous sphere held together by self-gravitation, a so-called polytrope [25]. These model stars are constructed from hydrostatic equilibrium

$$\frac{dp}{dr} = -\rho \frac{d\phi}{dr} \tag{3.11}$$

and Poisson's equation in spherical symmetry

$$\frac{1}{r^2} \frac{d}{dr} \left(r^2 \frac{d\phi}{dr} \right) = 4\pi G \rho, \tag{3.12}$$

where r is the radial variable and G is the gravitational constant.

Table 4
Error in density and pressure for the three-dimensional polytrope computed with the unbalanced/balanced second-order schemes.

N	Density	Pressure
32	1.29E–2/1.52E–14	7.07E–03/1.49E–15
64	3.62E–3/2.97E–14	2.50E–03/3.00E–15
128	1.03E–3/5.61E–14	8.41E–04/9.60E–15
Rate	1.82/–	1.54/–

With help of the polytropic relation $p = K\rho^\gamma$ and assuming K constant, Eqs. (3.11) and (3.12) can be combined into a single equation

$$\frac{1}{r^2} \frac{d}{dr}\left(r^2 \gamma K \frac{d\rho}{dr}\right) = -4\pi G \rho, \tag{3.13}$$

which is known as the Lane–Emden equation. For three ratios of specific heats ($\gamma = 6/5, 2, \infty$) the Lane–Emden equation can be solved analytically (see e.g. [25]).

We will use $\gamma = 2$ since neutron stars can be modeled by $\gamma = 2$–3 and since there exists an analytical solution to (3.13). The density and pressure are then given by

$$\rho(r) = \rho_c \frac{\sin(\alpha r)}{\alpha r}, \qquad p(r) = K\left(\rho_c \frac{\sin(\alpha r)}{\alpha r}\right)^2 \tag{3.14}$$

where

$$\alpha = \sqrt{\frac{4\pi G}{2K}} \tag{3.15}$$

and ρ_c is the central density of the polytrope. The gravitational potential is given by

$$\phi(r) = -2K\rho_c \frac{\sin(\alpha r)}{\alpha r}. \tag{3.16}$$

Note that the polytrope (obviously) fulfills $h(r) + \phi(r) = 0 = const$ for any $r \geqslant 0$. In the following, we set $K = G = \rho_c = 1$ for the model constants.

We then initialized the density, pressure profile (3.14) and gravitational potential (3.16) onto a Cartesian domain of size $(x, y, z) \in [-0.5, 0.5]^3$ uniformly discretized by N^3 grid cells. The radius is given by $r^2 = x^2 + y^2 + z^2$. The velocity is set to zero in the full domain. We apply the one-dimensional boundary conditions in Section 3.1 for density, pressure and velocity. The boundary conditions are applied in each direction and the gravitational potential in the boundary is given by the analytical solution. We note that the initialized hydrostatic configuration fulfills the discrete equilibrium $h(x, y, z) + \phi(x, y, z) = 0 = const$ exactly.

3.2.1. Well-balanced property

We first check the behavior of the well-balanced and unbalanced second-order schemes on the stationary polytrope. We evolved the model star with $N = 32, 64, 128$ for 20 sound crossing times, i.e. $t_f = 20\tau_{sound} \approx 14.8$. The errors in density and pressure are summarized in Table 4. We observe that the well-balanced scheme produces errors on the order of the machine (double) precision. Hence, the scheme is indeed well-balanced. However, the unbalanced scheme suffers from large spurious perturbations.

3.2.2. Small amplitude wave propagation

In order to test the capability of the schemes to evolve small perturbations of the hydrostatic equilibrium, we add a small Gaussian hump in pressure to the model star of the previous test:

$$p(r) = K\rho(r)^2 + Ae^{-100r^2},$$

where $\rho(r)$ is given by (3.14). We set the amplitude to $A = 10^{-3}$.

We evolved the initial conditions up to time $t = 0.2$ just before the excited waves reach the boundary. As a reference, we computed the same test problem in one-dimensional spherical symmetry using the second-order well-balanced scheme and $N = 8192$ cells. The errors in pressure and radial velocity are shown in Table 5. We observe that the well-balanced scheme shows roughly three orders of magnitude smaller errors in pressure and velocity than the unbalanced scheme. Moreover, we note that the errors in pressure and velocity for the well-balanced scheme on the coarsest resolution are smaller than the respective errors of the unbalanced scheme on the finest resolution. This underlines the superiority and computational efficiency of well-balanced schemes for the simulation of small disturbances on top of a stationary state.

Table 5
Error in pressure and velocity for a small pressure perturbation of the three-dimensional polytrope computed with the unbalanced/balanced second-order schemes.

N	Pressure	Velocity
32	8.40E–04/1.07E–06	5.96E–04/8.79E–07
64	2.06E–04/3.68E–07	1.59E–04/2.96E–07
128	5.09E–05/1.05E–07	4.14E–05/8.45E–08
Rate	2.02/1.67	1.92/1.69

(a) Pressure perturbation   (b) Velocity
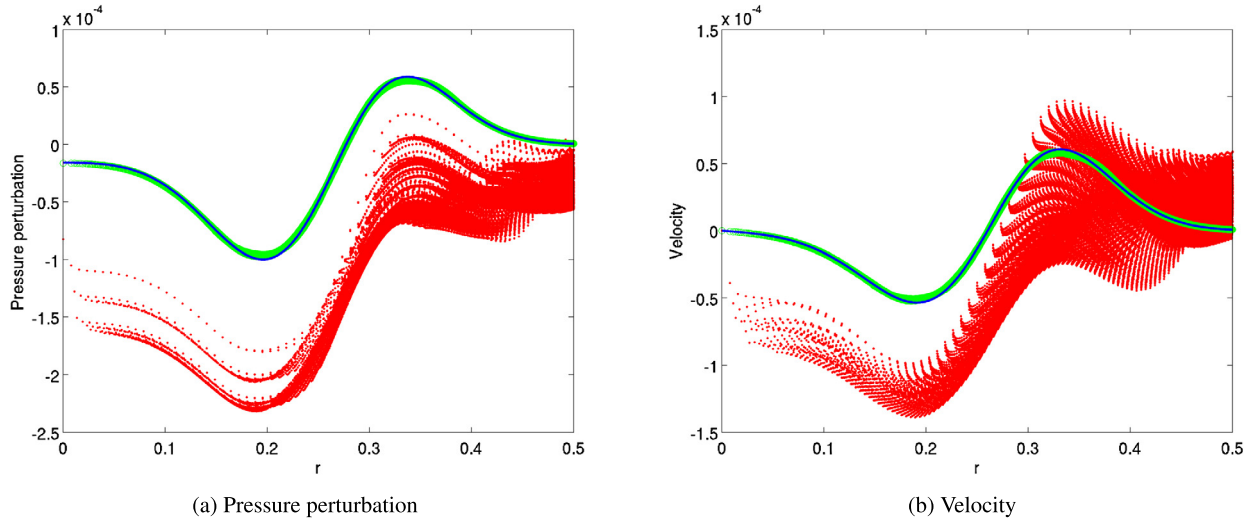
Fig. 4. Small pressure perturbation of the three-dimensional polytrope. In the left panel is shown a scatter plot of the pressure perturbation (pressure at final time minus the pressure of the unperturbed polytrope) as a function of radius. The right panel displays a scatter plot of the radial velocity as a function of radius. The red/green dots correspond to the computation with the unbalanced/balanced second-order schemes and $N^3 = 128^3$. The solid blue line represents the reference solution obtained from a high resolution one-dimensional computation. (For interpretation of the references to color in this figure legend, the reader is referred to the web version of this article.)

In Fig. 4 are displayed a scatter plot of the pressure perturbation (pressure at final time minus the pressure of the unperturbed polytrope) and the radial velocity as a function of radius. The red/green dots represent the values computed with the unbalanced/balanced second-order schemes at resolution $N^3 = 128^3$. The solid blue line is the reference obtained from a one-dimensional high resolution computation. We observe that the well-balanced scheme resolves the wave pattern very well. On the other hand, the unbalanced scheme suffers from spurious deviations.

3.2.3. Explosion
Next we check the shock capturing properties of the multi-dimensional well-balanced scheme. To this end, we start again from the polytrope. In the center of the computational domain, i.e $r \leqslant r_1 = 0.1$, we increase the equilibrium pressure by a factor $\alpha = 10$

$$p(r) = \begin{cases} \alpha K \rho(r)^2, & r \leqslant r_1, \\ K \rho(r)^2, & r > r_1, \end{cases}$$

triggering an explosion.

This setup was evolved up to time $t = 0.15$. A scatter plot of the pressure and radial velocity as a function of radius for the unbalanced/balanced second-order scheme (red/green dots) are shown in Fig. 5. As a reference, the result of a one-dimensional computation assuming spherical symmetry with $N = 8192$ cells is also shown (blue solid line). The over pressurized central region quickly expands driving a first strong shock wave outward. However, as the shock wave moves out, gravity starts to pull back some matter behind it, driving a collapse which then eventually leads to a rebound in the center. This rebound then drives another outward running shock wave. In Fig. 5, this cycle has been repeated twice (hence the two strong shock waves) and is about to happen again as matter is pulled back (the negative velocities below $r \approx 0.1$). Due to the very strong perturbation, the unbalanced and well-balanced schemes give virtually identical results. In Table 6, we display the errors in pressure and velocity with both schemes. We observe that the unbalanced and well-balanced schemes show a rate of convergence close to one and the errors are of comparable magnitude. Therefore we conclude that the hydrostatic reconstruction does not diminish the robustness of the base shock capturing scheme.

Table 6
Error in pressure and velocity for the explosion of the three-dimensional polytrope computed with unbalanced/balanced second-order schemes.

N	Pressure	Velocity
32	3.31E–02/3.28E–02	2.86E–02/2.79E–02
64	1.80E–02/1.80E–02	1.46E–02/1.44E–02
128	9.57E–03/9.54E–03	7.59E–03/7.55E–03
Rate	0.90/0.89	0.96/0.94

(a) Pressure   (b) Velocity
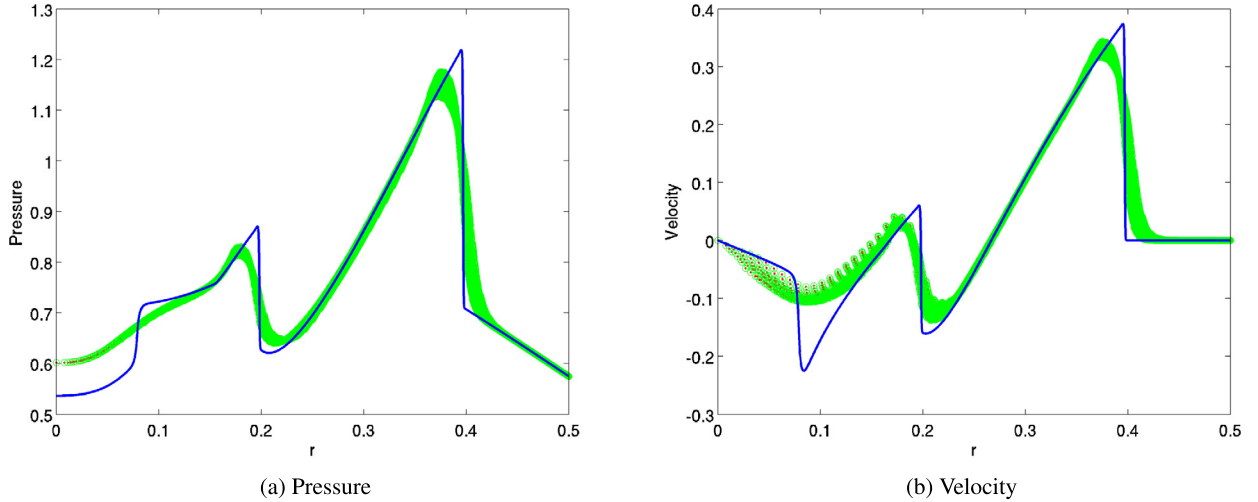
Fig. 5. Explosion of the three-dimensional polytrope. In the left/right panel is shown a scatter plot of the pressure/velocity as a function of radius. The red/green dots correspond to the computation with the unbalanced/balanced second-order schemes. Note that the two computations are nearly indistinguishable by eye, as to be expected for this strong perturbation. The solid blue line represents the reference solution obtained from a high resolution one-dimensional computation. (For interpretation of the references to color in this figure legend, the reader is referred to the web version of this article.)

3.2.4. Rayleigh–Taylor instability

Next, we simulate the development of the Rayleigh–Taylor instability within the three-dimensional polytrope. The Rayleigh–Taylor instability is a fluid instability occurring when gravity is acting on a denser fluid lying above a lighter fluid. For this purpose, we use a density distribution given by

$$\rho(r) = \sqrt{\frac{K}{\tilde{K}(r)}} \rho_c \frac{\sin(\alpha r)}{\alpha r},$$

where

$$\tilde{K}(r) = \begin{cases} 1, & r \leqslant r_{RT}, \\ 0.9, & r > r_{RT} \end{cases}$$

and $r_{RT} = 0.25$. The pressure and gravitational potential distributions are left unaltered. This introduces a density jump $\Delta\rho \approx 0.05$ at r_{RT}. The initial density profile is depicted in the right panel of Fig. 6 with the solid blue line. We introduce a single mode perturbation of the instability by the following velocity field

$$\mathbf{v}(r) = A\big(1 + \cos(20\phi)\big)\big(1 + \cos(20\theta)\big)\exp\left(-\frac{10^3}{r_{RT}}(r - r_{RT})^2\right)\mathbf{e}_r,$$

where $A = 0.05$ is the amplitude of the perturbation, $\mathbf{e}_r = [x, y, z]^T/r$ the radial unit vector, θ the polar angle and ϕ the azimuthal angle. We treat this problem up to time $t = 1.5$ in the first octant, $(x, y, z) \in [0, 0.5]^3$, with reflecting boundary conditions on the coordinate planes. For a clear distinction between the light and the heavy fluid, we include a passively advected quantity q, evolved by
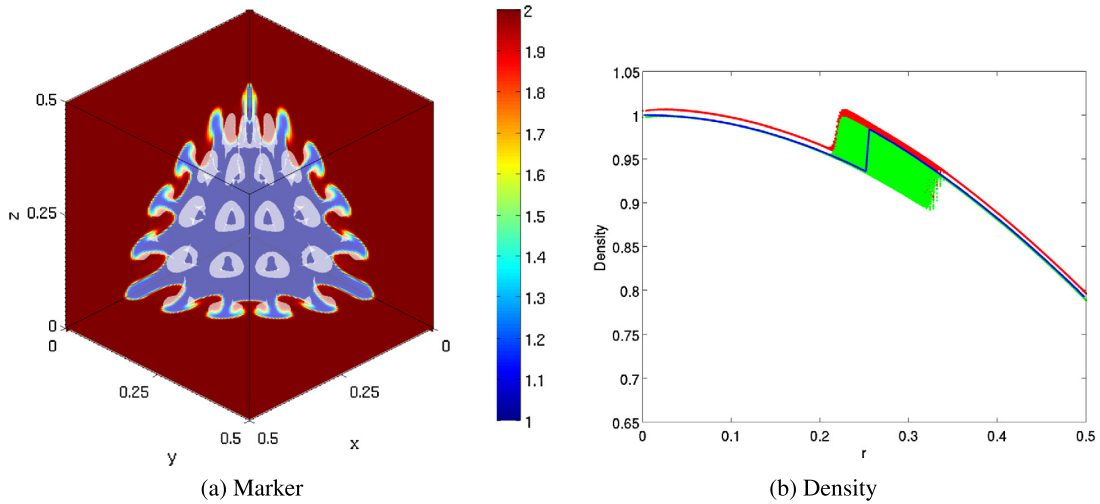
$$\frac{\partial \rho q}{\partial t} + \nabla \cdot \rho q \mathbf{v} = 0,$$

and initial distribution

$$q = \begin{cases} 1, & r \leqslant r_{RT}, \\ 2, & r > r_{RT}. \end{cases}$$

Hence, the light fluid has $q = 1$ and the heavy $q = 2$, respectively.

(a) Marker   (b) Density

Fig. 6. Rayleigh–Taylor instability within the three-dimensional polytrope. (For interpretation of the references to color in this figure legend, the reader is referred to the web version of this article.)

We run this problem with the unbalanced/balanced second-order schemes and 128^3 uniform grid cells. The result is shown in Fig. 6. The left panel shows a contour of the passively advected variable q for the three coordinate planes together with an isocontour $q = 1.5$ computed with the well-balanced scheme. One observes the development of several Rayleigh–Taylor mushrooms. The right panel shows a scatter plot of the density as a function of radius for the unbalanced/well-balanced scheme (red/green dots) together with the initial density profile (solid blue line). The well-balanced scheme maintains the hydrostatic state very well and the flow motions is restricted around the unstable interface. The unbalanced scheme is also able to capture the Rayleigh–Taylor instability, but also suffers from large spurious deviations from the equilibrium away from the unstable interface.

3.3. Three-dimensional white dwarf

As a final test, we present the performance of the well-balanced schemes on a problem involving a complex multiphysics equation of state (EoS). The test consists of the simulation of small and large amplitude pressure perturbations in a model white dwarf. White dwarfs are the final evolutionary state of stars that are not massive enough to become a neutron star [26].

The construction of a model white dwarf starts from the self-gravitating hydrostatic equilibrium in spherical symmetry given by (3.11) and (3.12). Instead of the ideal gas law, we employ an EoS which is more applicable to stellar environments. We use the stellar EoS thoroughly described in [27], which includes contributions of (photon) radiation, nuclei, electrons and positrons. The radiation is treated as a blackbody in local thermodynamic equilibrium and the nuclei are modeled by an ideal gas. The electrons and positrons are treated in a tabular manner together with a thermodynamically consistent interpolation procedure. We use the publicly available version of this EoS [28].

We set $\rho_c = 2 \times 10^9$ g cm^{-3} and $T_c = 5 \times 10^8$ K for the white dwarf's central density and temperature, respectively. We assume a constant entropy profile and the composition is set to half carbon ^{12}C and half oxygen ^{16}O. The model white dwarf is then computed by integrating numerically

$$\frac{dp}{dr} = -\rho G \frac{M(r)}{r^2},$$

where

$$M(r) = \int_0^r 4\pi r^2 \rho \, dr$$

is the enclosed mass and G is the gravitational constant. We set $G = 6.674 \times 10^{-8}$ cm^3 g^{-1} s^{-2}. Furthermore, the gravitational potential, given by

$$\phi(r) = \int_0^r G \frac{M(r)}{r^2} \, dr,$$
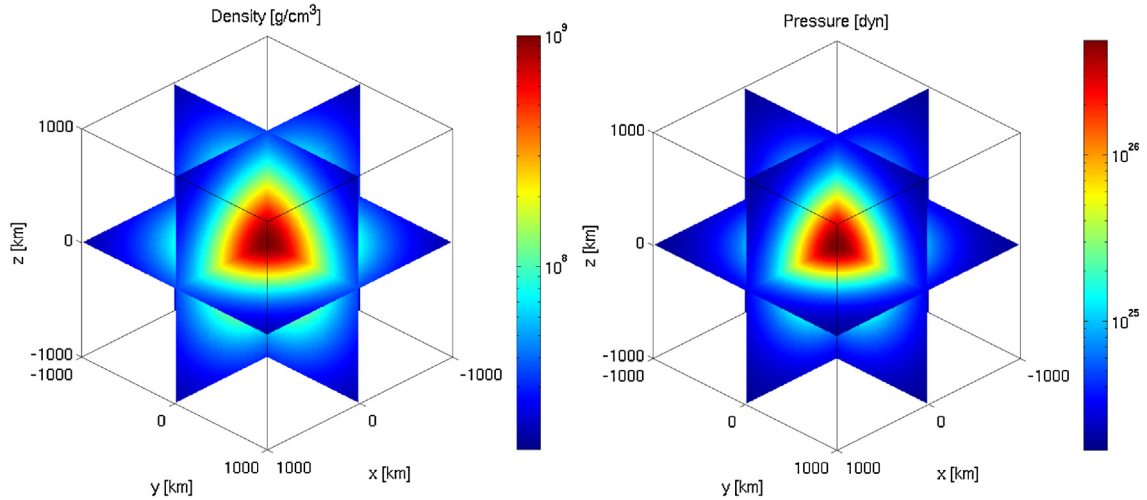
is also computed by numerical integration.

Fig. 7. Density (left) and pressure (right) coordinate plane contours for the unperturbed white dwarf setup.

We map the numerically obtained pressure $p(r)$, density $\rho(r)$ and gravitational potential $\phi(r)$ profiles onto a Cartesian domain $[-D/2, D/2]^3$, $D = 2000$ km, uniformly discretized by $N^3 = 128^3$ cells. The velocity is set to zero. We employ the same boundary conditions as for the three-dimensional polytrope Section 3.2. The initial white dwarf data are illustrated in Fig. 7.

For the EoS we use here, all state variables are computed as a function of temperature and density. Given a temperature and a density, the remaining essential thermodynamic variables, namely the pressure, the specific energy, entropy and enthalpy, are calculated from the EoS. Moreover, the partial derivatives with respect to temperature and density can also be calculated from the EoS.

As we solve the Euler equations in conservation form, we have to find the temperature corresponding to the specific internal energy $e = e(T, \rho) = (E - \rho v^2/2)/\rho$, in order to compute the pressure $p = p(T, \rho)$. Furthermore, in our reconstruction process (which is in terms of the primitive variables), the temperatures $T_{i\pm1/2\mp}$ corresponding to the cell interface extrapolated specific internal energies $e_{i\pm1/2\mp} = e(T_{i\pm1/2\mp}, \rho_{i\pm1/2\mp})$ have to be calculated. These temperatures are calculated iteratively with a *one-dimensional* Newton–Raphson scheme.

The usage of a complex EoS in the well-balanced schemes is straightforward. The only difficulty relies in the computation of the state variables (density, pressure, specific internal energy), given the specific enthalpy and entropy. For the EoS used here, one needs to compute the temperature and density that correspond to a given specific enthalpy $h = h(T, \rho)$ and entropy $s = s(T, \rho)$. This can be achieved iteratively with a *two-dimensional* Newton–Raphson scheme in every cell.

The computational cost of the well-balanced schemes with general EoS is higher, because systems of two non-linear equations have to be solved in the equilibrium reconstruction. In contrast, the standard unbalanced schemes have to solve only single non-linear equations. This moderate increase in computational cost is well compensated by the gain in resolution with the method, as demonstrated in the following discussion.

In the following we present simulations of small and large amplitude pressure perturbations. We do not repeat the well-balanced property test for brevity.

### 3.3.1. Small amplitude wave propagation

To demonstrate the ability of the well-balanced schemes to evolve small perturbations of hydrostatic equilibrium, we add a small Gaussian hump pressure perturbation in the center of the white dwarf:

$$p(r) = \left(1 + A e^{-\frac{r^2}{2b^2}}\right) p_0(r),$$

where $p_0(r)$ is the equilibrium profile, $A = 10^{-3}$ the perturbation amplitude and $b = 100$ km the width of the perturbation.

The initial conditions were then evolved up to time $t = 7.32 \times 10^{-2}$ s with the unbalanced and the well-balanced second-order schemes. Fig. 8 shows scatter plots of the pressure perturbation (pressure at final time minus pressure of the unperturbed white dwarf) and the radial velocity as a function of radius. The red/green dots have been computed with the unbalanced/well-balanced schemes, respectively. The solid blue line is a reference solution obtained from a one-dimensional high resolution simulation.

From the figure it is clear, that the unbalanced scheme is totally unable to capture the pressure perturbation. On the other hand, the well-balanced scheme resolves the perturbation very well. As a matter of fact, the solution computed with the well-balanced scheme is nearly indistinguishable from the reference solution. The figure also demonstrates the computational efficiency of the well-balanced schemes for this type of problems. To obtain a comparable result, the standard

(a) Pressure perturbation
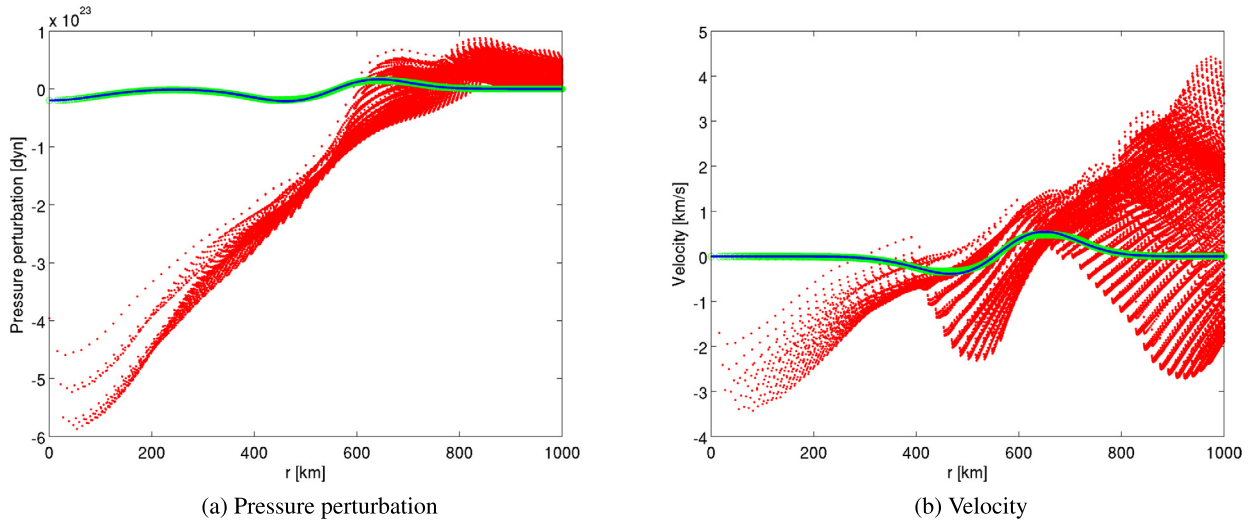
(b) Velocity

Fig. 8. Small pressure perturbation of the white dwarf. Scatter plots of the pressure perturbation (left) and velocity (right) for the unbalanced (red dots) and well-balanced (green dots) second-order schemes. The blue solid line is a reference solution obtained by a high resolution one-dimensional computation. (For interpretation of the references to color in this figure legend, the reader is referred to the web version of this article.)

(a) Pressure
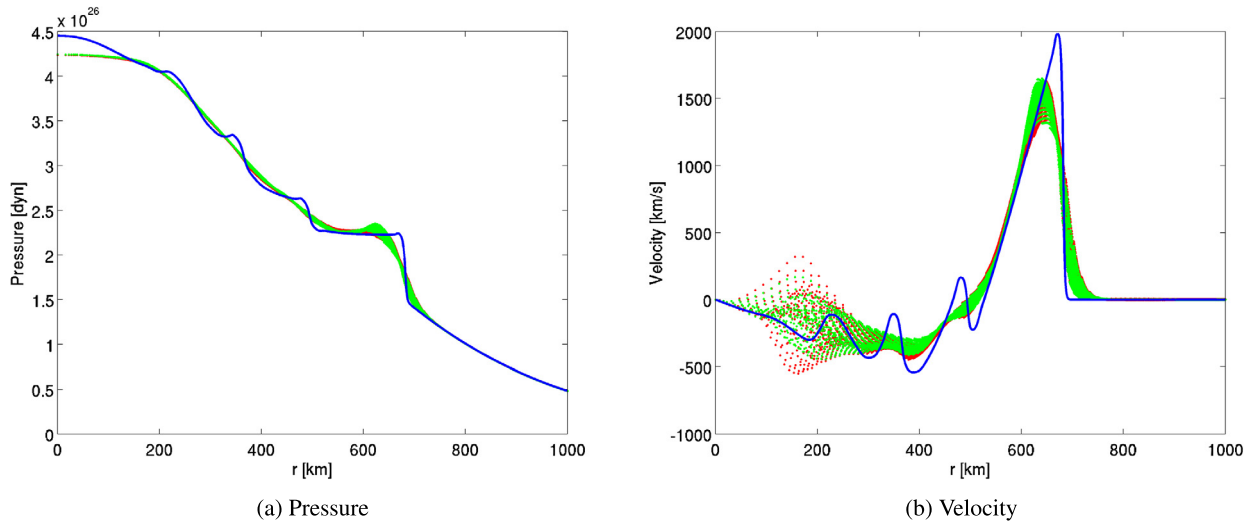
(b) Velocity

Fig. 9. Large pressure perturbation of the white dwarf. Scatter plots of the pressure (left) and velocity (right) for the unbalanced (red dots) and well-balanced (green dots) second-order schemes. The blue line is a reference solution obtained by a high resolution one-dimensional computation. (For interpretation of the references to color in this figure legend, the reader is referred to the web version of this article.)

unbalanced scheme needs a much higher resolution. Hence, the higher computational cost of the simulation with the well-balanced scheme outweighs by far the cost of an equally accurate simulation with standard schemes.

3.3.2. Explosion

To demonstrate the robustness of the well-balanced scheme with a general EoS, we introduce a small over pressurized region in the center of the white dwarf

$$p(r) = \begin{cases} \alpha p_0(r), & r \leqslant r_1, \\ p_0(r), & r > r_1, \end{cases}$$

where $\alpha = 10$, $r_1 = 100$ km and $p_0(r)$ is the equilibrium pressure profile.

The expansion of the over pressurized region is then computed up to time $t = 5.49 \times 10^{-2}$ s. Scatter plots of the pressure and the velocity as a function of radius are shown in Fig. 9. From the figure we observe, that the well-balanced scheme is comparable to the unbalanced scheme. This is to be expected for such large equilibrium perturbations. Hence, we conclude that the well-balanced scheme is as robust as the standard scheme also in the case of a general EoS.

4. Conclusion

The Euler equations with gravitation arise in many physical models such as in numerical weather prediction, climate modeling and in astrophysics as in the propagation of waves in the outer solar atmosphere or in the simulation of core-collapse supernovae. Many problems of interest require the robust numerical approximation of small perturbations on top of hydrostatic equilibrium steady states. Standard finite volume schemes can resolve these interesting steady state only within the truncation error. Hence, they are deficient at efficiently approximating small perturbations (smaller than truncation error on realistic grids) of these steady states. Consequently, one is interested in designing well-balanced schemes that exactly preserve discrete hydrostatic equilibria and can resolve small perturbations on top of them.

In this paper, we design a new class of well-balanced schemes for the Euler equations with gravitation that exactly preserve a discrete equilibrium for a large class of stable hydrostatic equilibria. The key design principle is based on the observation that a local relation between the enthalpy and the gravitational potential hold for such equilibria and this relation can be utilized within a local hydrostatic reconstruction procedure. Since the hydrostatic reconstruction is built from a standard thermodynamical potential, the schemes are well-balanced for more complex equations of state than the ideal gas law. The well-balanced schemes can handle any form of the gravitational potential including the one prescribed by the solution of Poisson's equation, i.e. self-gravity. This make the corresponding schemes applicable for a broad set of astrophysical scenarios including e.g. core-collapse supernova explosions. Both first- and second-order schemes are designed and the scheme is extended to be well-balanced with respect to multi-dimensional equilibria.

A set of numerical experiments illustrating the robustness of the well-balanced schemes is also presented. The numerical experiments are shown for both one and three spatial dimensions and include an example of a self-gravitating model star. The numerical experiments demonstrate that the well-balanced schemes preserve a discrete steady state to machine precision whereas an *unbalanced* standard scheme only preserves them at the level of the truncation error. Hence, testing with small amplitude perturbations (on top of the discrete equilibrium) shows that the well-balanced scheme provides a significantly lower error than the unbalanced scheme. This fact necessitates the use of well-balanced schemes for resolving near steady flows and complex flows that might contain regions which are small amplitude perturbations of a steady state. Furthermore, for large amplitude perturbations, the well-balanced scheme is comparable in performance with the unbalanced scheme demonstrating its robust shock capturing abilities.

The current paper deals with a very large class of stable steady states. However, there might be some situations of interest where only a mechanical equilibrium may hold. The design of well-balanced schemes for those steady states (particularly in several space dimensions) is quite complicated on account of certain geometric constraints. Well-balanced schemes with respect to such equilibria will be dealt with in a forthcoming paper. Furthermore, well-balanced schemes as presented here, will be coupled with other interesting physical effects to enhance the robustness of supernova simulations in forthcoming papers.

Acknowledgement

Appendix A. Proof of Theorem 1: Consistency of the momentum source term

To complete the proof of momentum source consistency, we have to show that

$$A = \frac{1}{\Delta x}\sum_{k\geqslant 2}\frac{1}{k!}\left(\Delta h_{i+}^{k} - (-1)^{k}\Delta h_{i-}^{k}\right) = \frac{1}{\Delta x}\sum_{k\geqslant 2}\frac{(-1)^{k}}{k!}\left(\left(\phi(x_{i+1/2}) - \phi_{i}\right)^{k} - (-1)^{k}\left(\phi_{i} - \phi(x_{i-1/2})\right)^{k}\right)\frac{\partial^{k}p}{\partial h^{k}}(h_{i}^{n})$$

is of order $O(\Delta x^2)$. Assuming that the gravitational potential is smooth, we expand the cell interface gravitational potential in Taylor series as follows

$$A = \frac{1}{\Delta x}\sum_{k\geqslant 2}\frac{(-1)^{k}}{k!}\left[\left(\phi_{i} + \sum_{l\geqslant 1}\frac{1}{l!}\left(\frac{\Delta x}{2}\right)^{l}\frac{\partial^{l}\phi}{\partial x^{l}} - \phi_{i}\right)^{k} - (-1)^{k}\left(\phi_{i} - \phi_{i} - \sum_{l\geqslant 1}\frac{1}{l!}\left(-\frac{\Delta x}{2}\right)^{l}\frac{\partial^{l}\phi}{\partial x^{l}}\right)^{k}\right]\frac{\partial^{k}p}{\partial h^{k}}(h_{i}^{n})$$

$$= \frac{1}{\Delta x}\sum_{k\geqslant 2}\frac{(-1)^{k}}{k!}\underbrace{\left[\left(\sum_{l\geqslant 1}\frac{1}{l!}\left(\frac{\Delta x}{2}\right)^{l}\frac{\partial^{l}\phi}{\partial x^{l}}\right)^{k} - \left(\sum_{l\geqslant 1}\frac{1}{l!}\left(-\frac{\Delta x}{2}\right)^{l}\frac{\partial^{l}\phi}{\partial x^{l}}\right)^{k}\right]}_{=:(*)}\frac{\partial^{k}p}{\partial h^{k}}(h_{i}^{n})$$

Now let us focus on the term $(*)$ defined in the last equality. We truncate the Taylor expansion of the gravitational potential to some arbitrary degree N and then apply the multinomial theorem:

$$(*) = \left(\sum_{l=1}^{N}\left(\frac{\Delta x}{2}\right)^{l}\frac{1}{l!}\frac{\partial^{l}\phi}{\partial x^{l}}\right)^{k} - \left(\sum_{l=1}^{N}\left(-\frac{\Delta x}{2}\right)^{l}\frac{1}{l!}\frac{\partial^{l}\phi}{\partial x^{l}}\right)^{k}$$

$$
= \sum_{\sum_{l=1}^{N} m_l = k} \binom{k}{m_1, m_2, \ldots, m_N} \left(\left(\frac{\Delta x}{2} \right) \frac{\partial \phi}{\partial x} \right)^{m_1} \cdot \left(\left(\frac{\Delta x}{2} \right)^2 \frac{1}{2} \frac{\partial^2 \phi}{\partial x^2} \right)^{m_2} \cdot \cdots \cdot \left(\left(\frac{\Delta x}{2} \right)^N \frac{1}{N!} \frac{\partial^N \phi}{\partial x^N} \right)^{m_N}
$$

$$
- \sum_{\sum_{l=1}^{N} m_l = k} \binom{k}{m_1, m_2, \ldots, m_N} \left(\left(-\frac{\Delta x}{2} \right) \frac{\partial \phi}{\partial x} \right)^{m_1} \cdot \left(\left(-\frac{\Delta x}{2} \right)^2 \frac{1}{2} \frac{\partial^2 \phi}{\partial x^2} \right)^{m_2} \cdot \cdots \cdot \left(\left(-\frac{\Delta x}{2} \right)^N \frac{1}{N!} \frac{\partial^N \phi}{\partial x^N} \right)^{m_N}
$$

$$
= \sum_{\sum_{l=1}^{N} m_l = k} \binom{k}{m_1, m_2, \ldots, m_N} \left(\left(\frac{\Delta x}{2} \right) \frac{\partial \phi}{\partial x} \right)^{m_1} \cdot \left(\left(\frac{\Delta x}{2} \right)^2 \frac{1}{2} \frac{\partial^2 \phi}{\partial x^2} \right)^{m_2} \cdot \cdots
$$

$$
\cdot \left(\left(\frac{\Delta x}{2} \right)^N \frac{1}{N!} \frac{\partial^N \phi}{\partial x^N} \right)^{m_N} \left(1 - (-1)^{m_1 + 2m_2 + \cdots + Nm_N} \right)
$$

$$
= \sum_{\sum_{l=1}^{N} m_l = k} \binom{k}{m_1, m_2, \ldots, m_N} \left(\frac{\partial \phi}{\partial x} \right)^{m_1} \cdot \left(\frac{1}{2} \frac{\partial^2 \phi}{\partial x^2} \right)^{m_2} \cdot \cdots
$$

$$
\cdot \left(\frac{1}{N!} \frac{\partial^N \phi}{\partial x^N} \right)^{m_N} \left(\frac{\Delta x}{2} \right)^{m_1 + 2m_2 + \cdots + Nm_N} \left(1 - (-1)^{m_1 + 2m_2 + \cdots + Nm_N} \right).
$$

From the last equality we see that the summands with $m_1 + 2m_2 + \cdots + Nm_N$ even vanish. This shows that $(*)$ is an odd power of Δx and hence $(*)/\Delta x$ is always an even power of Δx. Because the later is valid for any expansion truncated at arbitrary degree N this is valid in general. Since in A, $k \geqslant 2$, it follows that A is an even power in Δx starting at degree 2.

References

[1] C.M. Dafermos, Hyperbolic Conservation Laws in Continuum Physics, Grundlehren Math. Wiss. (Fundam. Principles Math. Sci.), vol. 325, Springer-Verlag, Berlin, 2000.
[2] R.J. LeVeque, Finite Volume Methods for Hyperbolic Problems, 1st ed., Camb. Texts Appl. Math., Cambridge University Press, 2002.
[3] L.D. Landau, E.M. Lifschitz, W. Weller, Lehrbuch der theoretischen Physik, 10 Bde., Bd.6, Hydrodynamik, Deutsch (Harri), 1991.
[4] N. Botta, R. Klein, S. Langenberg, S. Lützenkirchen, J. Comput. Phys. 196 (2004) 539.
[5] F. Fuchs, A. McMurry, S. Mishra, N. Risebro, K. Waagan, J. Comput. Phys. 229 (2010) 4033.
[6] R. LeVeque, J. Sci. Comput. 1 (2010).
[7] H.-T. Janka, K. Langanke, A. Marek, G. Martínez-Pinedo, B. Müller, Phys. Rep. 442 (2007) 38.
[8] J. Greenberg, A. Leroux, SIAM J. Numer. Anal. 33 (1996) 1.
[9] R.J. LeVeque, J. Comput. Phys. 146 (1998) 346.
[10] E. Audusse, F. Bouchut, M.-O. Bristeau, R. Klein, B. Perthame, SIAM J. Sci. Comput. 25 (2004) 2050.
[11] M. Castro, J.M. Gallardo, C. Parés, Math. Comput. 75 (2006) 1103.
[12] D. Kröner, M.D. Thanh, SIAM J. Numer. Anal. 43 (2005) 796.
[13] P.G. Lefloch, M.D. Thanh, Commun. Math. Sci. 1 (2003) 763.
[14] S. Noelle, N. Pankratz, G. Puppo, J.R. Natvig, J. Comput. Phys. 213 (2006) 474.
[15] S. Noelle, Y. Xing, C.-W. Shu, J. Comput. Phys. 226 (2007) 29.
[16] R.J. LeVeque, D.S. Bale, in: Proc. 7th Intl. Conf. on Hyperbolic Problems, 1998.
[17] Y. Xing, C.-W. Shu, J. Sci. Comput. 54 (2013) 645.
[18] C.B. Laney, Computational Gasdynamics, Cambridge University Press, 1998.
[19] E.F. Toro, Riemann Solvers and Numerical Methods for Fluid Dynamics. A Practical Introduction, Springer-Verlag GmbH, 1997.
[20] P. Batten, N. Clarke, C. Lambert, D.M. Causon, SIAM J. Sci. Comput. 18 (1997) 1553.
[21] B. van Leer, J. Comput. Phys. 32 (1979) 101.
[22] A. Harten, B. Engquist, S. Osher, S.R. Chakravarthy, J. Comput. Phys. 71 (1987) 231.
[23] C.-W. Shu, S. Osher, J. Comput. Phys. 83 (1989) 32.
[24] S. Gottlieb, C.-W. Shu, E. Tadmor, SIAM Rev. 43 (2001) 89.
[25] S. Chandrasekhar, An Introduction to the Study of Stellar Structure, Dover, New York, 1967.
[26] S.L. Shapiro, S.A. Teukolsky, Black Holes, White Dwarfs, and Neutron Stars, Wiley-VCH Verlag GmbH, 2007.
[27] F.X. Timmes, F.D. Swesty, Astrophys. J. Suppl. Ser. 126 (2000) 501.
[28] F.X. Timmes, http://cococubed.asu.edu/code_pages/eos.shtml, 2013.